The Cryosphere Discuss., 9, 2867–2913, 2015
www.the-cryosphere-discuss.net/9/2867/2015/
doi:10.5194/tcd-9-2867-2015

The Cryosphere Discussions
Open Access

Changing surface–atmosphere energy exchange and refreezing capacity of the lower accumulation area, west Greenland

C. Charalampidis[1,2], D. van As[1], J. E. Box[1], M. R. van den Broeke[3], W. T. Colgan[1], M. MacFerrin[4], H. Machguth[1,5], and P. P. Smeets[3]

[1]Geological Survey of Denmark and Greenland (GEUS), Øster Voldgade 10, 1350 Copenhagen K, Denmark
[2]Department of Earth Sciences, Uppsala University, Villavägen 16, 752 36 Uppsala, Sweden
[3]Institute for Marine and Atmospheric research (IMAU), Utrecht University, P.O. Box 80005, 3508TA Utrecht, the Netherlands
[4]Cooperative Institute for Research in Environmental Sciences (CIRES), 216 UCB, University of Colorado Boulder, Boulder, CO 80309, USA
[5]Arctic Technology Centre (ARTEK), Technical University of Denmark, Brovej, byg. 118, 2800 Kgs. Lyngby, Denmark

Received: 19 March 2015 – Accepted: 27 April 2015 – Published: 27 May 2015

Correspondence to: C. Charalampidis (cc@geus.dk)

Published by Copernicus Publications on behalf of the European Geosciences Union.

Abstract

We present five years (2009–2013) of automatic weather station measurements from the lower accumulation area (1840 m a.s.l.) of the ice sheet in the Kangerlussuaq region, western Greenland. Here, the summers of 2010 and 2012 were both exceptionally warm, but only 2012 resulted in a strongly negative surface mass budget (SMB) and surface meltwater runoff. The observed runoff was due to a large ice fraction in the upper 10 m of firn that prevented meltwater from percolating to available pore volume below. Analysis reveals a relatively low 2012 summer albedo of ~ 0.7 as meltwater was present at the surface. Consequently, during the 2012 melt season the surface absorbed 29 % (213 MJ m^{-2}) more solar radiation than the average of all other years.

A surface energy balance model is used to evaluate the seasonal and interannual variability of all surface energy fluxes. The model reproduces the observed melt rates as well as the SMB for each season. A sensitivity test reveals that 71 % of the additional solar radiation in 2012 was used for melt, corresponding to 36 % (0.64 m) of the 2012 surface lowering. The remaining 1.14 m was primarily due to the high atmospheric temperatures up to +2.6 °C daily average, indicating that 2012 would have been a negative SMB year at this site even without the melt-albedo feedback.

Longer time series of SMB, regional temperature and remotely sensed albedo (MODIS) show that 2012 was the first strongly negative SMB year with the lowest albedo at this elevation on record. The warm conditions of the last years resulted in enhanced melt and reduction of the refreezing capacity at the lower accumulation area. If high temperatures continue the current lower accumulation area will turn into a region with superimposed ice in coming years.

TCD
9, 2867–2913, 2015

1 Introduction

Glaciers and ice caps have dominated the cryospheric component to global average sea level rise during the past century (0.5 mm yr^{-1}, i.e. about 70 % of the total cryospheric component for the period 1961–2003; Solomon et al., 2007) due to their relatively short response times to climate variability. However, the largest freshwater reservoir in the Northern Hemisphere is the Greenland ice sheet, which would cause a sea level rise of 7.4 m if completely melted (Bamber et al., 2013). The average sea level rise contribution from the ice sheet has increased from 0.09 mm yr^{-1} over the period 1992–2001 to 0.6 mm yr^{-1} over the period 2002–2011, according to the latest IPCC report (Vaughan et al., 2013). The sheer volume of the ice sheet and the relatively large warming of the polar regions may yield an increasingly dominant contribution to cryospheric mass loss in coming decades.

An increasingly important driver of this accelerating mass loss is surface melt and subsequent runoff (Shepherd et al., 2012). Between 2009 and 2012, roughly 84 % of the increased Greenland ice sheet's mass loss was due to enhanced surface runoff (Enderlin et al., 2014), causing a reduction of the surface mass budget (SMB; Ettema et al., 2009, 2010). Increased melt is primarily the result of atmospheric warming (Huybrechts et al., 2011; Huybrechts and de Wolde, 1999) and the darkening of the ice sheet (Bøggild et al., 2010; Box et al., 2012; Van As et al., 2013; Wientjes and Oerlemans, 2010). An increase in meltwater production is commonly expected to be largely compensated for by water refreezing in snow and firn (Harper et al., 2012). However, it is suggested that in a moderate warming scenario the ice sheet will lose 50 % of its capacity to retain water by the end of the century (Van Angelen et al., 2013).

In-situ measurements are essential for understanding the impact of the changing atmospheric conditions on the ice sheet. In the Kangerlussuaq region, West Greenland, seven automatic weather stations (AWS) and nine SMB stakes constitute a relatively dense network of in situ measurements (Van de Wal et al., 1995; Greuell et al., 2001; Van den Broeke et al., 2008a; Van As et al., 2012). The uppermost

TCD
9, 2867–2913, 2015

AWS, KAN_U, was established on 4 April 2009 (67°0′0″ N, 47°1′1″ W; Fig. 1). Located approximately 140 km inland from the ice margin and at about 1840 m a.s.l., KAN_U is one of the few AWS in Greenland located in the lower accumulation area, where small changes in climate forcing will have the largest impact on the ice sheet surface.

In the Kangerlussuaq region, approximately 150 km of mountainous tundra separates the ice sheet from the ocean. Characteristic for the ice sheet in this region is a relatively wide (approx. 100 km) ablation area. The equilibrium line altitude (ELA), where annual accumulation and ablation are equal, was estimated to be 1535 m a.s.l. for the period of 1990–2003 (Van de Wal et al., 2005), but is reported to have increased (1553 m a.s.l. for 1990–2011; Van de Wal et al., 2012). At 1520 m a.s.l., superimposed ice becomes apparent at the surface at the end of every ablation season and its upglacier extent is estimated until about 1750 m a.s.l. (Van den Broeke et al., 2008a). The percolation area is found at higher elevations up to about 2500 m a.s.l., the lower limit of the dry snow area.

The ablation area in this region has been studied extensively. Van den Broeke et al. (2008a) presented four years of radiation measurements below the ELA. The lowest albedo values are found at the intermediate AWS S6 (1020 m a.s.l.) due to the surface-melt-water-induced "dark band" (Greuell, 2000; Wientjes and Oerlemans, 2010). Melt modelling revealed the increase of summer melt toward the margin and the decreasing role of sensible heat flux with increasing elevation, but also the increasing dominance of shortwave radiation in the surface energy balance (SEB) during melt at higher elevations (Van den Broeke et al., 2008b, 2011). An annual cycle in surface roughness length was found to exist over a large part of the ablation area (Smeets and van den Broeke, 2008). This determines part of the variability in the turbulent heat fluxes during the summer months as presented by Van den Broeke et al. (2009). This study showed that the katabatic nature of the wind over the region, in combination with the variable surface roughness in the lower regions, provides significant year-round turbulent heat transfer in a stable surface layer. An increasing wind speed with surface elevation was identified, contrary to what would be expected from katabatically

TCD
9, 2867–2913, 2015

forced wind over an ice surface flattening with elevation. This is due to the larger surface roughness near the margin (Smeets and van den Broeke, 2008), the increasing influence of the large scale pressure gradient force (Van Angelen et al., 2011) and the proximity of pooled cold air over the tundra that sets up an opposing pressure gradient force in the boundary layer during winter. Van As et al. (2012) quantified the extreme surface melt in the Kangerlussuaq region in 2010, validated by river discharge measurements.

At elevations above the superimposed ice area and below the dry snow area (i.e. ∼ 1750–2500 m a.s.l.), sufficient melt occurs to impact snow/firn properties, but not enough to reveal bare ice. In a warming climate with melt at increasingly high elevations, this area would comprise an increasingly large portion of the ice sheet due to the ice sheet's flattening with increasing elevation. A rare event in July 2012 caused melt at all elevations of the ice sheet (Nghiem et al., 2012). Bennartz et al. (2013) attributed this Greenland-wide event of increased near-surface temperatures partially to thin, low-level liquid clouds. These clouds, while optically thick and low enough to enhance downward longwave radiation, were thin enough for solar radiation to reach the surface. They were present at Summit station about 30 % of the time during the 2012 summer months.

A large difference with the ablation area is that in the accumulation area, processes within the snow/firn layers such as meltwater percolation and refreezing significantly impact the mass budget (Harper et al., 2012). Additionally, an important process is the melt-albedo feedback (Box et al., 2012). Our aim is to assess the SMB sensitivity to atmospheric forcing in the lower accumulation area using AWS measurements that serve as input for a SEB model. The five-year period with AWS measurements (2009–2013) spans a wide range of melting conditions, including the record melting years of 2010 and 2012 (Tedesco et al., 2011, 2013; Van As et al., 2012; Nghiem et al., 2012; Hanna et al., 2014) and years with limited melting such as 2009 and 2013. We add temporal perspective by discussing Kangerlussuaq temperatures since 1976 and Moderate Resolution Imaging Spectroradiometer (MODIS) albedo values since 2000.

TCD
9, 2867–2913, 2015

In the following, we first describe the observations and SEB calculations, after which we will present the atmospheric conditions and surface energy fluxes at KAN_U, and the changes therein due to recent years with extreme melt. Finally, we investigate the importance of the melt-albedo feedback on the SMB of the lower accumulation area and discuss how changes in the firn can yield SMB variability on a short, interannual time scale.

2 Methods

2.1 AWS measurements

KAN_U is part of the network of ∼ 20 AWSs in the Programme for Monitoring of the Greenland Ice Sheet (PROMICE; Ahlstrøm et al., 2011). Measurements include ambient air pressure, relative humidity and aspirated temperature (T_a) at 2.7 m height above surface, wind speed and direction at 3.1 m, as well as incoming and reflected solar/shortwave ($E_S^{\downarrow}$, $E_S^{\uparrow}$) and downward and emitted terrestrial/longwave ($E_L^{\downarrow}$, $E_L^{\uparrow}$) radiation components at 10 min intervals. Accumulation and ablation are measured by two sonic rangers, one attached to the AWS and one on a separate stake assembly (Fig. 1b). Sensor specifications are listed in Table 1. The AWS transmits hourly measurements during the summer period and daily during winter.

AWSs installed on glaciers are prone to tilt due to the changes of the ice or firn surface. The importance of accounting for the pyranometer tilt has been discussed by e.g. MacWhorter and Weller (1991). AWSs located in accumulation areas are comparatively stable due to the accumulated snow on the base of the tripod. The maximum tilt registered by KAN_U is 3.0°. A tilt correction for the solar radiation measurements is made after Van As (2011).

Two gaps in (sub)hourly measurements exist due to a malfunctioning memory card, from 27 October 2010 until 22 April 2011 and from 26 October 2011 until 21 January 2012. During these periods with only transmitted daily values, measurements

TCD
9, 2867–2913, 2015

from a second AWS, S10, erected on 17 August 2010 at ∼ 50 m distance were used, adjusted by linear regression to prevent e.g. offsets due to a difference in measurement height. The overlapping time series of the two time series revealed high cross-correlations and low root-mean-square deviations (RMSD) for every measured parameter (Table 2). Due to technical issues with S10, $E_L^{\downarrow}$, $E_L^{\uparrow}$ and T_a measurement gaps from 9 February 2011 until 30 April 2012 were filled with a similar approach, using measurements from AWS S9 located 53 km closer to the ice sheet margin. Any added uncertainty from using adjusted wintertime measurements will have minimal impact on the summertime results presented below.

The broadband albedo is the fraction of the incoming shortwave radiation reflected at the surface and an important parameter in studying the changes in the accumulation area:

$$\alpha = \left| \frac{E_S^{\uparrow}}{E_S^{\downarrow}} \right| . \quad (1)$$

To verify its accuracy, albedo was compared for both AWSs KAN_U and S10 for the warm seasons (May–September) of 2010, 2011 and 2012 (Table 2). For hourly values, the RMSD for 2010 and 2011 was only ∼ 0.03. The RMSD for 2012 was 0.07, due to the larger spatial variability in surface reflectance after substantial melt.

2.2 Surface radiation budget

The radiation budget at the surface is given by the sum of solar and terrestrial radiation components:

$$E_R = E_S^{\downarrow} + E_S^{\uparrow} + E_L^{\downarrow} + E_L^{\uparrow} = E_S^{\mathrm{Net}} + E_L^{\mathrm{Net}} . \quad (2)$$

Fluxes are here taken as positive when directed toward the surface. By the inclusion of albedo and utilizing the Stefan–Boltzmann law, this can be rewritten as:

$$E_R = (1 - \alpha)E_S^{\downarrow} + \varepsilon E_L^{\downarrow} - \varepsilon\sigma T_S^4 \quad (3)$$

TCD
9, 2867–2913, 2015

with σ being the Stefan–Boltzmann constant ($5.67\times10^{-8}\,\mathrm{W\,m^{-2}\,K^{-4}}$) and T_S the surface temperature. The longwave emissivity ε for snow/firn is assumed equal to 1 (black-body assumption).

2.3 SEB model

Various studies have applied SEB models in glaciated areas under different climatic conditions (e.g. high Antarctic plateau, Van As et al., 2005; Greenland ablation area, Van den Broeke et al., 2008b, 2011). The energy balance at the atmosphere–surface interface is:

$$E_M = E_R + E_H + E_E + E_G + E_P\,, \tag{4}$$

where E_H, E_E, E_G and E_P are the turbulent sensible, turbulent latent, subsurface conductive and rain-induced energy fluxes, respectively.

Rainfall is assumed to be at melting-point temperature ($T_0 = 273.15\,\mathrm{K}$), thus E_P is non-zero when T_s is below freezing:

$$E_P = \rho_w c_w \dot{r}(T_0 - T_s)\,, \tag{5}$$

where c_w is the specific heat of water ($4.21\,\mathrm{kJ\,kg^{-1}\,K^{-1}}$ at 0 °C) and $\dot{r}$ is the rainfall rate. The latter is assumed non-zero when conditions of heavy cloud cover during periods with non-freezing air temperatures are met (see below).

The energy balance is solved for the one unknown variable T_s. If T_s is limited to the melting-point temperature (273.15 K), the imbalance in Eq. (4) is attributed to melt (E_M). For sub-freezing T_s values all other SEB components are in balance and surface melt does not occur. E_H and E_E are calculated using the "bulk method" as described by Van As et al. (2005). This method uses atmospheric stability, and thus depends on T_s, implying that Eq. (4) has to be solved iteratively.

The average surface roughness length for momentum z_0 at this elevation would realistically be $\sim 10^{-4}$ m (Smeets and van den Broeke, 2008). During summer, the

TCD
9, 2867–2913, 2015

surface melts occasionally, smoothing it and thus attaining a smaller z_0 ($\sim 10^{-5}$ m). Slightly increased roughness is expected during wintertime due to sastrugi, and drifting snow can increase z_0 in cases up to 10^{-3} m (Lenaerts et al., 2014). In the present study, z_0 is kept constant at 10^{-4} m. A series of test runs showed that the results of this study were not very sensitive in the range of plausible z_0 values. The scalar roughness lengths for heat and moisture are calculated according to Andreas (1987).

Subsurface heat transfer is calculated on a 200 layer grid with 0.1 m spacing (20 m total) and is forced by temperature changes at the surface and latent heat release when water refreezes within the firn. Heat conduction is calculated using effective conductivity as a function of firn density (Sturm et al., 1997) and specific heat of firn as a function of temperature (Yen, 1981). The calculations are initialized using thermistor string temperatures from April 2009 and depth-adjusted firn core densities measured on 2 May 2012. The subsurface part of the model includes a percolation/refreezing scheme based on Illangasekare et al. (1990), assuming active percolation within snow/firn. Provided that there is production of meltwater at the surface, the amount of refreezing is limited either by the available pore volume or by the available cold content at each level. The scheme simulates water transport and subsequent refreezing as the progression of a uniform warming front into the snow/firn and is active for all melt seasons except for 2012. In 2012, surface runoff dominates water movement after 14 July, as clearly visible on Landsat imagery (not shown). This coincided with the surfacing of a 6 m thick ice layer in the model, which was also found in firn cores (Machguth et al., 2015). Here we use 6 m of ice (density of 900 kg m^{-3}) as a threshold that causes meltwater to run off horizontally, shutting down vertical percolation.

Solid precipitation is added in the model based on KAN_U sonic ranger measurements, assuming snow density of 400 kg m^{-3} in accordance to snow pit measurements. Although rain occurs only sporadically at 1840 m a.s.l., a rain estimate is incorporated with prescribed precipitation rates for each year during hours with a thick cloud cover producing $E_L^{\downarrow}$ values that exceed black-body radiation using the air temperature ($E_L^{\downarrow} > \sigma T_a^4$) and T_a is above freezing. Testing this against winter

TCD
9, 2867–2913, 2015

accumulation, the following precipitation rates were found and applied to the rain calculation: 2.0×10^{-3} m h^{-1} for 2009–2010 and 2012–2013, 3.5×10^{-3} m h^{-1} for 2010–2011 and 0.5×10^{-3} m h^{-1} for 2011–2012. Using this approach, the model produces liquid precipitation during the summer months only; by the end of the five-year period it amounts to a total of 0.26 m, 15 % of the total precipitation over the five years. The contribution of rain in the energy balance is minor; the total energy added to the surface for the whole study period is approximately 1.15 MJ m^{-2}, which could yield a total of 9 mm of melted snow.

The performance of the model in terms of ablation is illustrated by comparing the simulated with the measured surface height change due to ablation and accumulation in Fig. 2a. The model accurately reproduces the melt rates during every melt season. Yet this validation does not cover the whole melt season. We found that the AWS tripod and stake assembly are prone to sinking somewhat into warm, melting firn during the second part of the melt season (note the measurement gaps). In a second model validation method we compare the simulated with the measured T_s (inferred from the $E_L^{\uparrow}$) in Fig. 2b, and find they correlate well ($R^2 = 0.98$) with an average difference of 0.11 °C and root-mean-square error (RMSE) of 1.43 °C. Part of the difference can be attributed to the seemingly overestimated 10 % $E_L^{\uparrow}$ measurement uncertainty as reported by the sensor manufacturer, which would yield a RMSE of 6.2 °C of T_s values.

2.4 Additional measurements

For a study with a five-year time span, it is useful to provide a longer temporal perspective. For this, we use North Atlantic Oscillation (NAO) index measurements from the National Oceanic and Atmospheric Administration (NOAA). We use the air temperature record from Kangerlussuaq airport by the Danish Meteorological Institute (DMI), initiated in 1973 to facilitate flight operations (Cappelen, 2013). Full observational coverage is available from 1976. Monthly T_a from the airport correlate well with the KAN_U time series ($R = 0.97$), indicating that Kangerlussuaq

TCD
9, 2867–2913, 2015

measurements can be used for providing temporal perspective in spite of the 160 km distance that separates the two measurement sites. Finally, from 5 km × 5 km regridded MODIS albedo measurements (MOD10A1) we use the pixel nearest to KAN_U to investigate albedo variability in a 2000–2013 perspective.

3 Results

3.1 Meteorological observations

The importance of katabatic and synoptic forcing on near-surface wind direction is roughly equally important at the elevation of KAN_U (Van Angelen et al., 2011). The average wind direction is south-southeast (∼ 150°; Fig. 3a). Yet, in a case study of the 2012/13 winter (Van As et al., 2014), the prevailing wind direction of ∼ 135° (southeast) suggests an influential katabatic regime in which air drains down-slope, deflected by Coriolis forcing. Wind speed is higher during winter (Fig. 3b); annual average values are 6–7 m s^{-1} whereas summer average values are around 5 m s^{-1} (Table 3). Winds exceeding 15 m s^{-1} occur primarily during the winter period and rarely exceed 20 m s^{-1} averaged over 24 h. The barometric pressure of about 800 hPa exhibits an annual cycle with relatively high pressure in summer (Fig. 3c), favoring more stable, clear-sky conditions. Also the specific humidity varies annually, peaking in summer. Annual values are about 1.5 g kg^{-1}.

The year 2010 was the warmest year of the record (Table 3), with the winter (December–January–February) of 2009–2010 being 4.0 °C warmer than the 2009–2013 average, and the summer (June–July–August) only being equaled by 2012 (−1.8 °C; Table 3). Especially May 2010 was warm at −6.2 °C, 5.1 °C above the 2009–2013 average. Positive T_a persisted during the end of the melt season resulting in a −1.1 °C monthly average for August. The high 2010 temperatures impacted the surface ablation inducing early onset, which lasted from late April until early September,

TCD
9, 2867–2913, 2015

whereas for instance the 2009 melt season at KAN_U occurred early June until mid-August.

The average SMB over the period 1994–2010 at KAN_U is +0.27 m w.e. (Van de Wal et al., 2012). Melt at this elevation occurs frequently during each melt season. The winter 2009–2010 accumulation was relatively low, amounting to 65 % of the 2009–2013 average (0.25 m w.e.; Table 4). During the 2010 melt season, all the accumulated snow since the end of the previous melt season ablated including part of the underlying firn, resulting in the first negative SMB year on record (Table 4). The stake measurements from Van de Wal et al. (2012) document a two-year surface height change of +0.42 m on average for 2008–2010 at the same location (S10), corresponding to +0.15 m w.e. assuming a snow pit density of 360 kg m^{-3}. From this estimate, we infer the winter and net SMB for 2009 to be +0.59 and +0.34 m w.e., respectively.

During winter 2011–2012, accumulation was the same as in winter 2009–2010. In spring 2012, positive T_a was first recorded during April (with −12.8 °C the warmest April on record), followed by a relatively warm May (−8.6 °C). Already in late May 2012 ablation rates were high (7.2 mm w.e. d^{-1}; Charalampidis and van As, 2015). June and July were the warmest of the five-year record with −1.5 and −0.6 °C monthly average T_a, respectively. With the summer of 2012 on average as warm as that of 2010, but the ablation period shorter by 38 days (Table 4), the summer SMB was −0.86 m w.e., making 2012 a strongly negative SMB year (−0.61 m w.e.) to be recorded at this location (Van de Wal et al., 2005, 2012).

3.2 Surface energy fluxes

Solar radiation exhibits a strong annual cycle at this location on the polar circle (Fig. 4a). In the absence of topographic shading or a significant surface slope (∼ 0.37°) the day-to-day variability in incoming shortwave radiation at this elevation is dominated by cloudiness and the solar zenith angle. The highest daily $E_S^{\downarrow}$ values occur in June and

TCD
9, 2867–2913, 2015

exceed 400 W m^{-2}, while at the ELA they are just below 400 W m^{-2} (Van den Broeke et al., 2008a) due to more frequent cloud cover and a thicker overlying atmosphere. Whereas $E_S^{\downarrow}$ increases with elevation from the ELA to KAN_U, E_S^{Net} obtains values of up to 100 W m^{-2} both at the ELA and at KAN_U, implying regulated solar energy input by surface reflectance.

Terrestrial radiation exhibits an annual cycle of smaller amplitude (Fig. 4a). The annual variations of the downward and emitted longwave radiation are governed by the temperature and emissivity variations of the atmosphere and the surface, respectively. Hence, the absolute magnitudes of both components are larger during the summer period. $E_L^{\downarrow}$ fluctuations depend primarily on cloud cover. $E_L^{\uparrow}$ is a sink to the SEB and during summer is limited by the melting surface with the maximum energy loss being 316 W m^{-2}. This results in predominantly negative E_L^{Net} values throughout the year. The energy loss peaks during June and July.

The E_R annual cycle displays an energy gain at the surface during May to August and energy loss the rest of the year (Fig. 4b). This winter energy loss is primarily compensated by downward sensible heat flux. Calculated E_H is typically positive throughout the year, with highest values in winter when E_R is most negative, heating the surface while cooling the atmospheric boundary layer (Fig. 4b). This facilitates the katabatic forcing and thus enhances wind speed and further turbulent energy exchange between the atmosphere and surface. The contribution of E_H to melt is smaller than at lower elevations (Van den Broeke et al., 2011); the dominant melt energy source at KAN_U is E_R.

E_E changes sign from winter to summer, and is on average a small contributor to the annual SEB. During the summer period, E_E is comparable to E_H but with opposite sign, enabling surface cooling by sublimation and/or evaporation. In the winter, E_E is directed mostly toward the cold surface, resulting in heating from deposition.

The annually averaged E_G is mostly negative and of the same magnitude as E_E (3–4 W m^{-2}), but with no distinct annual cycle. Melt seasons with substantial refreezing

TCD
9, 2867–2913, 2015

exhibit increased positive summer-averaged E_G since the near-surface firn temperature is on average higher than T_s, leading to conductive heat transport toward the surface. Low E_G values in summer indicate limited refreezing in the firn just below the surface.

E_P is non-zero, but still negligible in summer, when positive air temperatures occur and thus precipitation is liquid.

3.3 Interannual variability of the SEB and implications for melt

With the exception of August 2009, when predominantly clear skies caused $E_S^{\downarrow}$ being $40\,W\,m^{-2}$ larger and $E_L^{\downarrow}$ $36\,W\,m^{-2}$ smaller than in the other years, monthly average values of $E_S^{\downarrow}$ at this site are fairly invariant (difference $< 25\,W\,m^{-2}$; Fig. 5a). Often E_R increases when clouds are present over an ice sheet; a so-called radiation paradox (Ambach, 1974), as it was observed in April 2012.

Figure 5b illustrates the annual cycle of monthly average albedo, not including the winter months October–February when shortwave radiation values are too low for accurate estimation, yet it is expected to attain fresh dry snow values (0.8–0.9). High albedo persists until May due to fresh snow deposits on the surface. An exception occurred during March and April 2013 when the monthly albedo of 0.78 suggests reduced precipitation input for a prolonged period and the presence of old, clean, dry snow on the surface (Cuffey and Paterson, 2010). In the years 2009–2011 and 2013 the albedo gradually decreased beginning late May and during the summer due to the effects of relatively high temperatures and melt on snow metamorphism. During summer, albedo still exceeded 0.75. While in August melt at KAN_U can still occur, this does not counteract the effect of snowfall events that increase the surface albedo.

The anomalously warm period in June and July 2012 (Fig. 3d) coincided with a larger decrease of surface albedo than in the other years. The combination of enhanced melting, heat-induced metamorphosis and firn saturation, reduced the albedo from 0.85 in April to 0.67 in July reaching a value that corresponds to the lower soaked facies close to the snow/firn line (Cuffey and Paterson, 2010). As a consequence, E_S^{Net}

TCD
9, 2867–2913, 2015

increased by approximately 25 W m^{-2} in June and July (32 %; Fig. 5c). This darkening thus functions as an amplifier of melt (Box et al., 2012; Van As et al., 2013), contributing to the large observed ablation rates (Table 4).

The largest longwave radiation surface emissions occurred during August 2010 and June–July 2012, approaching the theoretical limit of −316 W m^{-2} for a continuously melting surface (Fig. 6b). The concurrent high $E_L^{\downarrow}$ (Fig. 6a; Table 5) was related to high atmospheric temperatures. This caused E_L^{Net} in the summers 2010 and 2012 to exceed its value in other years (Table 5; Van As et al., 2012). While summer E_S^{Net} was similar in 2009 and 2010, E_R was about 60 % larger in 2010 than in 2009 due to atmospheric temperatures alone. During summer 2012, E_L^{Net} was similar as in 2010. The large E_S^{Net}, resulted in E_R 67 % higher than in 2010 (Table 5). The highest daily E_R attained 100 W m^{-2} on 9 July and coincided with the start of a Greenland-wide warm event. On 12 July, nearly the entire ice sheet surface was reported to melt (Nghiem et al., 2012), followed shortly after by the highest meltwater discharge in 56 years as can be concluded by the partial destruction of the 1956 Watson river bridge in Kangerlussuaq on 12 July 2012. Well above the long-term ELA at KAN_U, not only a strongly negative SMB was recorded in 2012, but it was the only year with a positive annual radiation budget (E_R = +4 W m^{-2}; Table 5).

E_H was largest during 2010 and smallest during 2011 (Table 5), the years of highest and lowest annual T_a, respectively (Table 3). Sensible heat transfer toward the surface was on average also low in 2012 owing to the cold winter months. The high July 2011 E_H was due to warm air advection that occurred over a cold surface, yielding large near-surface temperature gradients and thus sensible heat exchange (Fig. 7a). In the summer of 2013, when the temperatures remained relatively low, the surface exhibited the lowest sensible heat gain compared to the other melt seasons. In all, E_H did not contribute to SEB interannual variability as much as the radiative components.

Summer E_E values are correlated with the atmospheric pressure (R = 0.96) that influences the gradients in near-surface specific humidity and wind speed. In the

TCD
9, 2867–2913, 2015

summer of 2012, pressure and specific humidity were high (811 hPa and 3.7 g kg^{-1}, respectively; Table 3), while the wind speed was reduced, thus contributing to the lowest absolute E_E with the lowest cooling rates due to evaporation/sublimation. The maximum latent heat loss that year occurred in May. Thereafter, the moisture content in the near-surface air became relatively large, with E_E decreasing in absolute value until July. Summer 2013, was characterized by low pressure and specific humidity (804 hPa and 2.8 g kg^{-1}, respectively) resulting in high evaporation/sublimation rates especially in June and July (Fig. 7b).

Monthly E_G values were small and displayed small interannual variability especially in summer. The summers of 2010 and 2011 exhibited the most positive E_G as a consequence of substantial refreezing (Fig. 7c), impacting the near-surface temperature gradients in the firn. The summer average E_G values for 2009 and 2013 (Table 5) were lower due to the moderate melt seasons of smaller duration. E_G was lower in summer 2012 due to a warm surface conducting heat into the firn and the absence of refreezing.

The melt in 2009 and 2013 was similar with the largest E_M occurring in July and not exceeding 30 W m^{-2} (Fig. 8a). E_M peaked similarly in 2010 and 2011, in June reaching about 20 W m^{-2} and in July exceeding 35 W m^{-2}. May and August 2010 sustained significant melt in response to the warm atmospheric conditions (Van As et al., 2012). Both 2010 and 2012 exhibited significant melt in May (10 W m^{-2}). During summer 2012, E_M far exceeded all other years with e.g. a July value of 68 W m^{-2}, leading to the large ablation reported in Table 4.

There is a large dominance of the radiative fluxes over the interannual variability of melt at KAN_U, the variations in E_L^{Net} being most influential over the amount of available E_M in the years 2009–2011 and 2013. In 2012, it was the large E_S^{Net} that mainly contributed to the melt anomaly.

TCD
9, 2867–2913, 2015

3.4 Melt-albedo feedback

Figure 9a shows the total surface energy exchange for each month throughout the study period. It illustrates that E_S^{Net} and E_L^{Net} dominate the energy balance during the months May to September, while E_L^{Net} and E_H govern the SEB during wintertime (Fig. 9a). For the years 2009–2011 and 2013 the total energy in the summer months was 1250–1300 MJ m^{-2}. In July, when the energy input is largest, the years 2009 and 2013 exhibited a total amount of energy of 464 MJ m^{-2} while in the years 2010 and 2011 it reached 500 MJ m^{-2}. In 2012, the summer total energy was significantly higher exceeding 1500 MJ m^{-2}, while July alone reached 608 MJ m^{-2} with 183 MJ m^{-2} invested in melting. The total melt energy in 2012 amounted to 414 MJ m^{-2}.

Figure 9b illustrates the simulated mass fluxes at the surface (note the different *y* scales for positive and negative values). A total of 40 kg m^{-2} of mass loss occurs on average by the sum of sublimation and evaporation during spring and summer. Deposition amounts 10 kg m^{-2} each winter season. The total snowfall from April 2009 until September 2013 amounted $\sim$ 1500 kg m^{-2} (also Table 4). Up to the end of May 2012, all meltwater had accumulated internally through percolation into the firn, adding a mass of of 1158 kg m^{-2} (1020 kg m^{-2} from snowfall and 138 kg m^{-2} from rainfall). Due to ice layer blocking vertical percolation in summer 2012, 444 kg m^{-2} ran off, removing approximately 38 % of accumulated mass since April 2009.

The total amount of meltwater generated at the surface, equaling the sum of runoff and refreezing, amounted 1307 kg m^{-2} in 2012. As the calculated surface ablation was 860 kg m^{-2} (Table 4), 66 % (447 kg m^{-2}) of the produced meltwater was melted more than once during the ablation season. Essentially, 48 % (416 kg m^{-2}) of the total ablation was retained.

2010 was the first year on record during which surface ablation exceeded accumulation from the preceding winter at KAN_U (Table 4; Van de Wal et al., 2012). Even though atmospheric temperatures were high and the impact on ablation was large in 2010, the response of the snow surface was much larger in 2012, when ablation

TCD
9, 2867–2913, 2015

was more than three times larger than the accumulation. Albedo in 2012 dropped to 0.7 already in mid-June (Charalampidis and van As, 2015), implying substantial metamorphosis of the snow surface, while in all other years this value was reached only in July or August. The albedo reduced even more on 10 July (~ 0.6), signifying the saturation of the surface and the exposure of thick firn. Until 6 August, the albedo value corresponded to that of soaked facies close to the snow/firn line (Cuffey and Paterson, 2010). It should be noted that snowfall events increased the albedo during several periods in the summer season (Charalampidis and van As, 2015).

The average annual cycle in albedo of all years excluding 2012 was used to replace the low 2012 albedo in a model run to quantify the impact of a relatively dark surface on the SEB. Figure 10a shows the albedo anomaly of 2012, which started invoking enhanced ablation in late May/early June (Fig. 10b). At the end of August, the surface lowered an additional 0.64 m due to 58 % more melt energy compared to a situation with average albedo. The excess E_M from the melt-albedo feedback amounted to 152 MJ m^{-2}, while the excess E_S^{Net} supplied was 213 MJ m^{-2} (Fig. 10c). The remaining E_S^{Net} was consumed by other fluxes, primarily E_H. As the total surface ablation of 2012 was 1.78 m of surface height change (Fig. 2) the remaining 1.14 m was primarily due to the warm atmospheric conditions and similar to 2010 (1.21 m). This implies that the location would have experienced a negative SMB in 2012 even without the melt-albedo feedback.

4 Discussion

4.1 Uncertainties

Model performance is limited by the accuracy of the instruments of KAN_U as given in Table 1. The radiometer uncertainties are the largest, based on what is reported by the manufacturer (10 % for daily totals, although this is likely to be an overestimate, Van den Broeke et al., 2004). Nevertheless, the accurate simulation of surface temperature and

TCD
9, 2867–2913, 2015

snow ablation rates (Fig. 2) throughout the period of observations builds confidence in both the measurements and the model.

The model exhibits considerable sensitivity to the subsurface calculations, suggesting importance of pore volume and firn temperature, and how much more complicated SEB calculations are in the lower accumulation area than for bare ice in the ablation area. The model is able to capture the seasonal variations of temperature in the firn and calculated temperatures are commonly within 3.6 °C of those measured with an average of −0.3 °C (Fig. 11a). The shallow percolation of a wetting front in the firn is estimated at depths of 1–3 m in the years 2009 and 2013 (Fig. 11b), while in the years of larger melt, pore volume until 10 m depth is filled, possibly overestimating the percolation depth given the relative temperature buildup in the simulated firn below roughly 5 m depth (Fig. 11a). In particular for 2012, available simulated pore volume at ∼ 6 m is significantly affected by meltwater that percolates below the formed thick ice layer, which may indicate that the runoff threshold of a 6 m ice layer is an overestimate, highlighting the need for a better runoff criterion. Further investigation on this criterion, and inclusion of water content held in the firn by capillary forces, saturation of the surface and proximity of impermeable ice to the surface is necessary.

The fact that the subsurface calculations are initialized in 2009 by use of vertically shifted firn densities from a 2012 core does not influence the calculation of the surface energy fluxes and thus the outcome of this paper. Importantly, the timing that simulated runoff occurred in July 2012 is in agreement with satellite observations due to the runoff criterion, thereby providing confidence in realistic calculation of E_G.

Although the subsurface calculations are on a vertical grid of 10 cm (see also Sect. 2.3), there is loss of detail in the density profile with time due to the interpolation scheme that shifts the column vertically when it needs to account for surface height variations (Fig. 11c). Increased spatial resolution requires a finer temporal resolution to avoid model instability. Since this would also increase calculation time severely, while the calculated SEB would be unaffected, we accepted the loss of detail in density in this study. Nevertheless, during each melt season when refreezing is important to be

TCD
9, 2867–2913, 2015

accounted for, no loss of detail is expected near the surface since the column is shifted almost continuously upward.

Rainfall is known to occur during summer on the higher elevations of the ice sheet. The exact amount is unknown as in situ measurements for precipitation are rare and difficult. Therefore, the rainfall calculated by our model should be considered a first-order estimate. Nevertheless, the amount of rain is expected to be small and its effect on the SEB is negligible, as shown by the model results.

It is possible that other factors than heat-induced snow metamorphism and the presence of surface water contributed to the 2012 albedo anomaly. Such could be aerosol particles or impurities at the snow surface, effectively reducing its albedo (Doherty et al., 2013). Also, in cases of extreme melt, microbial activity can develop at the surface with the subsequent production of a dark-colored pigment (Benning et al., 2014).

4.2 Long-term perspective in temperature and albedo

The regional barometric pressure is linked to the NAO with KAN_U measurements exhibiting a negative correlation ($R = -0.72$ for monthly averages) with the NAO index. The correlation between the NAO index and pressure in west Greenland implies that the variability of the regional climate is partly controlled by the North Atlantic climate (Figs. 12a, b). For instance, warm summers on the ice sheet coincide with extended periods of negative NAO index. The Kangerlussuaq airport temperature record since 1976 was used to provide a temporal perspective to the KAN_U temperature in recent years (Fig. 12c). The standard deviations (SDs) reveal variability during the winter period of more than 10 °C while for the months of July and August SDs are ~ 2.0 °C. The temperature measurements reveal that the region has been warming on average starting in 1996 (not shown). Figure 12d illustrates this for 2000–2013; e.g. the summers (JJA) were 1.2 °C warmer than in the reference period 1976–1999. The warm 2010 and 2012 summer have an anomaly value of +1.9 and +1.8 °C, respectively. The high temperatures in recent years are most apparent for June when

TCD
9, 2867–2913, 2015

in 10 out of 14 years the 1976–1999 SD is exceeded. A further increase of the regional temperatures, as anticipated by climate models, will likely further increase the frequency of large melt events and the extent of each melt season, leading to conditions similar to or more extreme than in 2012 (McGrath et al., 2013).

The MOD10A1 time series from the years 2000–2013 shows an albedo decrease of 0.05–0.10 during the 14 years of measurements in response to the increased temperatures (Fig. 13). In particular, May albedo reached record low values in 2010 and 2012. July albedo is considerably lower in the years 2007–2013 than it was in the first half of the record. The exceptional surface conditions in July 2012 were also captured by MODIS with the lowest monthly albedo (~ 0.6) of the time series. The albedo in August is generally higher than in July due to snowfall, but the values remain sufficiently low to enhance melt.

Increased meltwater infiltration into the firn during events of increased melt has led to the formation of thick, near-surface ice lenses between 2 and 7 m, judging from the 2012 firn core. This contrasts the aquifers (i.e. liquid water storage) that are observed in the firn in southeast Greenland (Forster et al., 2014; Koening et al., 2014; Kuipers Munneke et al., 2014). The southwest ice sheet receives about one third of the annual precipitation amount in the southeast (Ettema et al., 2009), resulting in differences in thermal insulation of the infiltrated water and available pore volume. Persistent shallow refreezing on an interannual scale has led to the formation of thick impermeable ice enabling runoff in 2012 (Machguth et al., 2015).

The DMI measurements indicate that 2009 is representative of the reference period 1976–1999 (Fig. 11c; Van As et al., 2012). In summer 2010 the radiation budget was increased due to reduced $E_{\mathrm{L}}^{\mathrm{Net}}$ by $10\,\mathrm{W\,m^{-2}}$ (Table 5; Sect. 3.3). The concurrent increase in melt was $13\,\mathrm{W\,m^{-2}}$. In summer 2012, $E_{\mathrm{S}}^{\mathrm{Net}}$ was $17\,\mathrm{W\,m^{-2}}$ larger than in 2010, approximately 70 % of which was consumed by melting ($12\,\mathrm{W\,m^{-2}}$; Sect. 3.4). The melt-albedo feedback (Box et al., 2012) will contribute to the rise of the ELA in a warming climate (Fettweis, 2007; Van de Wal et al., 2012) and might transform the lower accumulation area into superimposed ice if warming prevails. We have shown

TCD
9, 2867–2913, 2015

that the melt-albedo feedback makes that warm summers can have great impact on melt and runoff in the lower accumulation area. Our results suggest that if warm atmospheric conditions persist in the future, the additional input of solar radiation at the surface will be of higher importance to surface changes than atmospheric warming.

5 Conclusions

We used five years of automatic weather station measurements to characterize the prevailing meteorology and surface energy fluxes at a location in the lower accumulation area of the southwest Greenland ice sheet. The analysis showed large control of the radiative components over the interannual variability, and mostly from net longwave radiation. The main contributor to melt is absorbed solar radiation, but for all but one year of observations this did not induce surface mass balance variability. This was not the case during the 2012 melt season, when the area attained unusually low albedo values (< 0.7) owing to large melt and the subsequent exposure of water-saturated, high-density firn. The consequential enhanced solar absorption along with warm atmospheric conditions resulted in intensified melt during the strongest negative surface mass budget year since 1994, and presumably since at least 1976 given the Kangerlussuaq temperature record. A sensitivity test with our energy balance model indicates that the melt-albedo feedback contributed an additional 58 % (152 MJ m^{-2}) to melt energy in 2012, though increased atmospheric temperatures alone would have yielded a negative surface mass budget as well.

Percolation of meltwater within snow and firn is generally considered to refreeze in firn at 1840 m a.s.l. on the ice sheet, which prevents runoff and therefore limits Greenland's contribution to sea level rise. This applies to all the higher elevations of the ice sheet that experience moderate melt and where deep percolation is possible. However, the lower accumulation area of the southwestern ice sheet showed high sensitivity to the warm atmosphere in 2012, primarily because of the relatively low precipitation in the region enables the immediate loss of pore volume in the upper

TCD
9, 2867–2913, 2015

meters of firn under extreme melting conditions. Water retained in the firn can lead to substantial density increase due to refreezing, which in warm years not only may function as a mechanism to block percolation, but also lowers the albedo and enhances melt, accelerating the transformation of the lower accumulation area into an ablation-dominated region. This highlights the importance of accurate modelling of percolation and refreezing within firn to be able to estimate the contribution from the Greenland ice sheet to sea level rise.

Acknowledgements. We thank Andreas Mikkelsen for collection of snow densities, Alun Hubbard and Samuel Doyle for retrieval of KAN_U weather station measurements and Robert Fausto, Filippo Calì Quaglia and Daniel Binder for valuable discussions. The KAN weather stations are financed by the Greenland Analogue Project (GAP) and operated by the Geological Survey of Denmark and Greenland (GEUS). We also acknowledge support from the Netherlands Polar Programme of the Netherlands Organization for Scientific Research, section Earth and Life Sciences (NWO/ALW). This is a publication in the framework of the Programme for Monitoring of the Greenland Ice Sheet (PROMICE) and contribution number 52 of the Nordic Centre of Excellence SVALI, "Stability and Variations of Arctic Land Ice", funded by the Nordic Top-level Research Initiative (TRI).

References

Ahlstrøm, A. P., van As, D., Citterio, M., Andersen, S. B., Nick, F. M., Gravesen, P., Edelvang, K., Fausto, R. S., Andersen, M. L., Kristensen, S. S., Christensen, E. L., Boncori, J. P. M., Dall, J., Forsberg, R., Stenseng, L., Hanson, S., and Petersen, D.: Final report for the establishment phase of the Programme for Monitoring of the Greenland Ice Sheet, Geological Survey of Denmark and Greenland, Copenhagen, Denmark, Report number 2011/118, 2011.

Ambach, W.: The influence of cloudiness on the net radiation balance of a snow surface with high albedo, J. Glaciol., 13, 73–84, 1974.

Andreas, E. L.: A theory for the scalar roughness and the scalar transfer coefficients over snow and sea ice, Bound.-Lay. Meteorol., 38, 159–184, doi:10.1007/BF00121562, 1987.

TCD
9, 2867–2913, 2015

Bamber, J. L., Griggs, J. A., Hurkmans, R. T. W. L., Dowdeswell, J. A., Gogineni, S. P., Howat, I., Mouginot, J., Paden, J., Palmer, S., Rignot, E., and Steinhage, D.: A new bed elevation dataset for Greenland, The Cryosphere, 7, 499–510, doi:10.5194/tc-7-499-2013, 2013.

Bennartz, R., Shupe, M. D., Turner, D. D., Walden, V. P., Steffen, K., Cox, C. J., Kulie, M. S., Miller, N. B., and Pettersen, C.: July 2012 Greenland melt extent enhanced by low-level liquid clouds, Nature, 496, 83–86, doi:10.1038/Nature12002, 2013.

Benning, L. G., Anesio, A. M., Lutz, S., and Tranter, M.: Biological impact on Greenland's albedo, Nat. Geosci., 7, 691, doi:10.1038/ngeo2260, 2014.

Bøggild, C. E., Brandt, R. E., Brown, K. J., and Warren, S. G.: The ablation zone in northeast Greenland: ice types, albedos, and impurities, J. Glaciol., 56, 101–113, doi:10.3189/002214310791190776, 2010.

Box, J. E., Fettweis, X., Stroeve, J. C., Tedesco, M., Hall, D. K., and Steffen, K.: Greenland ice sheet albedo feedback: thermodynamics and atmospheric drivers, The Cryosphere, 6, 821–839, doi:10.5194/tc-6-821-2012, 2012.

Cappelen, J.: Weather Observations from Greenland 1958–2012, Technical Report 13–11, Danish Meteorological Institute, Copenhagen, Denmark, 2013.

Charalampidis, C. and van As, D.: Observed melt season snowpack evolution on the Greenland ice sheet, Geol. Surv. Denmark Greenland Bull., in press, 2015.

Cuffey, K. M. and Paterson, W.: The Physics of Glaciers, 4th Edn., Butterworth-Heinemann, Elsevier, 704 pp., 2010.

Doherty, S. J., Grenfell, T. C., Forsström, S., Hegg, D. L., Brandt, R. E., and Warren, S. G.: Observed vertical redistribution of black carbon and other insoluble light-absorbing particles in melting snow, J. Geophys. Res.-Atmos., 118, 5553–5569, doi:10.1002/jgrd.50235, 2013.

Enderlin, E. M., Howat, I. M., Jeong, S., Noh, M.-J., van Angelen, J. H., and van den Broeke, M. R.: An improved mass budget for the Greenland ice sheet, Geophys. Res. Lett., 41, 866–872, doi:10.1002/2013GL059010, 2014.

Ettema, J., van den Broeke, M. R., van Meijgaard, E., van de Berg, W. J., Bamber, J. L., Box, J. E., and Bales, R. C.: Higher surface mass balance of the Greenland ice sheet revealed by high-resolution climate modeling, Geophys. Res. Lett., 36, L12501, doi:10.1029/2009GL038110, 2009.

Ettema, J., van den Broeke, M. R., van Meijgaard, E., and van de Berg, W. J.: Climate of the Greenland ice sheet using a high-resolution climate model – Part 2: Near-surface climate and energy balance, The Cryosphere, 4, 529–544, doi:10.5194/tc-4-529-2010, 2010.

TCD
9, 2867–2913, 2015

Fettweis, X.: Reconstruction of the 1979–2006 Greenland ice sheet surface mass balance using the regional climate model MAR, The Cryosphere, 1, 21–40, doi:10.5194/tc-1-21-2007, 2007.

Forster, R. R., Box, J. E., van den Broeke, M. R., Miège, C., Burgess, E. W., van Angelen, J. H., Lenaerts, J. T. M., Koenig, L. S., Paden, J., Lewis, C., Gogineni, S. P., Leuschen, C., and McConnell, J. R.: Extensive liquid melt water storage in firn within the Greenland ice sheet, Nat. Geosci., 7, 95–98, doi:10.1038/ngeo2043, 2014.

Greuell, W.: Melt water accumulation on the surface of the Greenland ice sheet: effect on albedo and mass balance, Geogr. Ann. A, 82, 489–498, doi:10.1111/j.0435-3676.2000.00136.x, 2000.

Greuell, W., Denby, B., van de Wal, R. S. W., and Oerlemans, J.: Correspondance., 10 years of mass-balance measurements along a transect near Kangerlussuaq, central west Greenland, J. Glaciol., 47, 157–158, 2001.

Hanna, E., Fettweis, X., Mernild, S. H., Cappelen, J., Ribergaard, M. H., Shuman, C. A., Steffen, K., Wood, L., and Mote, T. L.: Atmospheric and oceanic climate forcing of the exceptional Greenland ice sheet surface melt in summer 2012, Int. J. Climatol., 34, 1022–1037, doi:10.1002/joc.3743, 2014.

Harper, J., Humphrey, N., Pfeffer, W. T., Brown, J., and Fettweis, X.: Greenland ice-sheet contribution to sea-level rise buffered by melt water storage in firn, Nature, 491, 240–243, doi:10.1038/nature11566, 2012.

Henneken, E. A. C., Bink, N. J., Vugts, H. F., Cannemeijer, F., Meesters, A. G. C. A.: A case study of the daily energy balance near the equilibrium line on the Greenland ice sheet, Global Planet. Change, 9, 69–78, doi:10.1016/0921-8181(94)90008-6, 1994.

Huybrechts, P. and de Wolde, J.: The dynamic response of the Greenland and Antarctic ice sheets to multiple-century climatic warming, J. Climate, 12, 2169–2188, doi:10.1175/1520-0442(1999)012<2169:TDROTG>2.0.CO;2, 1999.

Huybrechts, P., Goelzer, H., Janssens, I., Driesschaert, E., Fichefet, T., Goosse, H., and Loutre, M. F.: Response of the Greenland and Antarctic Ice Sheets to multi-millennial greenhouse warming in the earth system model of intermediate complexity LOVECLIM, Surv. Geophys., 32, 397–416, doi:10.1007/s10712-011-9131-5, 2011.

Illangasekare, T. H., Walter, R. J., Meier Jr., M. F., and Pfeffer, W. T.: Modeling of melt water infiltration in subfreezing snow, Water Resour. Res., 26, 1001–1012, doi:10.1029/WR026i005p01001, 1990.

TCD
9, 2867–2913, 2015

Koenig, L. S., Miège, C., Forster, R. R., and Brucker, L.: Initial in situ measurements of perennial melt water storage in the Greenland firn aquifer, Geophys. Res. Lett., 41, 81–85, doi:10.1002/2013GL058083, 2014.

Kuipers Munneke, P., Ligtenberg, S. R. M., van den Broeke, M. R., van Angelen, J. H., and Forster, R. R.: Explaining the presence of perennial liquid water bodies in the firn of the Greenland Ice Sheet, Geophys. Res. Lett., 41, 476–483, doi:10.1002/2013GL058389, 2014.

Lenaerts, J. T. M., Smeets, C. J. P. P., Nishimura, K., Eijkelboom, M., Boot, W., van den Broeke, M. R., and van de Berg, W. J.: Drifting snow measurements on the Greenland Ice Sheet and their application for model evaluation, The Cryosphere, 8, 801–814, doi:10.5194/tc-8-801-2014, 2014.

Machguth, H., MacFerrin, M., van As, D., Box, J. E., Charalampidis, C., Colgan, W. T., Fausto, R. S., Meijer, H. A. J., Mosley-Thompson, E., and van de Wal, R. S. W.: Successive and intense melt rapidly decreases Greenland meltwater retention in firn, Nat. Clim. Change, in review, 2015.

MacWhorter, M. A. and Weller, R. A.: Error in measurements of incoming shortwave radiation made from ships and buoys, J. Atmos. Ocean. Tech., 8, 108–117, doi:10.1175/1520-0426(1991)008<0108:EIMOIS>2.0.CO;2, 1991.

McGrath, D., Colgan, W., Bayou, N., Muto, A., and Steffen, K.: Recent warming at Summit, Greenland: global context and implications, Geophys. Res. Lett., 40, 2091–2096, doi:10.1002/grl.50456, 2013.

Nghiem, S. V., Hall, D. K., Mote, T. L., Tedesco, M., Albert, M. R., Keegan, K., Shuman, C. A., DiGirolamo, N. E., and Neumann, G.: The extreme melt across the Greenland ice sheet in 2012, Geophys. Res. Lett., 39, L20502, doi:10.1029/2012GL053611, 2012.

Shepherd, A., Ivins, E. R., Geruo, A., et al.: A reconciled estimate of ice-sheet mass balance, Science, 338, 1183–1189, doi:10.1126/science.1228102, 2012.

Smeets, C. J. P. P. and van den Broeke, M. R.: Temporal and spatial variations of the aerodynamic roughness length in the ablation zone of the Greenland ice sheet, Bound.-Lay. Meteorol., 128, 315–338, doi:10.1007/s10546-008-9291-0, 2008.

Solomon, S., Qin, D., Manning, M., Chen, Z., Marquis, M., Averyt, K. B., Tignor, M., and Miller, H. L. (Eds.): IPCC, Climate Change 2007: The Physical Science Basis, Contribution of Working Group I to the Fourth Assessment Report of the Intergovernmental Panel on Climate Change, Cambridge University Press, Cambridge, UK, New York, NY, USA, 996 pp., 2007.

TCD
9, 2867–2913, 2015

Sturm, M., Holmgren, J., Köning, M., and Morris, K.: The thermal conductivity of seasonal snow, J. Glaciol., 43, 26–41, 1997.
Tedesco, M., Fettweis, X., van den Broeke, M. R., van de Wal, R. S. W., Smeets, C. J. P. P., van de Berg, W. J., Serreze, M. C., and Box, J. E.: The role of albedo and accumulation in the 2010 melting record in Greenland, Environ. Res. Lett., 6, 014005, doi:10.1088/1748-9326/6/1/014005, 2011.
Tedesco, M., Fettweis, X., Mote, T., Wahr, J., Alexander, P., Box, J. E., and Wouters, B.: Evidence and analysis of 2012 Greenland records from spaceborne observations, a regional climate model and reanalysis data, The Cryosphere, 7, 615–630, doi:10.5194/tc-7-615-2013, 2013.
Van Angelen, J. H., van den Broeke, M. R., and van de Berg, W. J.: Momentum budget of the atmospheric boundary layer over the Greenland ice sheet and its surrounding seas, J. Geophys. Res.- Atmos., 116, D10101, doi:10.1029/2010JD015485, 2011.
Van Angelen, J. H., Lenaerts, J. T. M., van den Broeke, M. R., Fettweis, X., and Meijgaard, E.: Rapid loss of firn pore space accelerates 21st century Greenland mass loss, Geophys. Res. Lett., 40, 2109–2113, doi:10.1002/grl.50490, 2013.
Van As, D.: Warming, glacier melt and surface energy budget from weather station observations in the Melville Bay region of northwest Greenland, J. Glaciol., 57, 208–220, doi:10.3189/002214311796405898, 2011.
Van As, D., van den Broeke, M. R., Reijmer, C. H., and van de Wal, R. S. W.: The summer surface energy balance of the high Antarctic plateau, Bound.-Lay. Meteorol., 115, 289–317, doi:10.1007/s10546-004-4631-1, 2005.
Van As, D., Hubbard, A. L., Hasholt, B., Mikkelsen, A. B., van den Broeke, M. R., and Fausto, R. S.: Large surface meltwater discharge from the Kangerlussuaq sector of the Greenland ice sheet during the record-warm year 2010 explained by detailed energy balance observations, The Cryosphere, 6, 199–209, doi:10.5194/tc-6-199-2012, 2012.
Van As, D., Fausto, R. S., Colgan, W. T., Box, J. E., and the PROMICE project team: darkening of the Greenland ice sheet due to the melt-albedo feedback observed at the PROMICE weather stations, Geological Survey of Denmark and Greenland Bulletin, 28, 69–72, 2013.
Van As, D., Fausto, R. S., Steffen, K., and the PROMICE project team: katabatic winds and piteraq storms: observations from the Greenland ice sheet, Geological Survey of Denmark and Greenland Bulletin, 31, 83–86, 2014.

TCD
9, 2867–2913, 2015

Van de Wal, R. S. W., Bintanja, R., Boot, W., van den Broeke, M. R., Conrads, L. A., Duynkerke, P. G., Fortuin, P., Henneken, E. A. C., Knap, W. H. L., Portanger, M., Vugts, H. F., and Oerlemans, J.: Mass balance measurements in the Søndre Strømfjord area in the period 1990–1994, Zeitschrift für Gletscherkunde und Glazialgeologie, 31, 57–63, 1995.

Van de Wal, R. S. W., Greuell, W., van den Broeke, M. R., Reijmer, C. H., and Oerlemans, J.: Surface mass-balance observations and automatic weather station data along a transect near Kangerlussuaq, Greenland, Ann. Glaciol., 42, 311–316, doi:10.3189/172756405781812529, 2005.

Van de Wal, R. S. W., Boot, W., Smeets, C. J. P. P., Snellen, H., van den Broeke, M. R., and Oerlemans, J.: Twenty-one years of mass balance observations along the K-transect, West Greenland, Earth Syst. Sci. Data, 4, 31–35, doi:10.5194/essd-4-31-2012, 2012.

Van den Broeke, M. R., van As, D., Reijmer, C., and van de Wal, R.: Assessing and improving the quality of unattended radiation observations in Antarctica, J. Atmos. Ocean. Tech., 21, 1417–1431, doi:10.1175/1520-0426(2004)021<1417:AAITQO>2.0.CO;2, 2004.

Van den Broeke, M. R., Smeets, C. J. P. P., Ettema, J., and Munneke, P. K.: Surface radiation balance in the ablation zone of the west Greenland ice sheet, J. Geophys. Res.-Atmos., 113, D13105, doi:10.1029/2007JD009283, 2008a.

Van den Broeke, M., Smeets, P., Ettema, J., van der Veen, C., van de Wal, R., and Oerlemans, J.: Partitioning of melt energy and meltwater fluxes in the ablation zone of the west Greenland ice sheet, The Cryosphere, 2, 179–189, doi:10.5194/tc-2-179-2008, 2008b.

Van den Broeke, M. R., Smeets, C. J. P. P., and Ettema, J.: Surface layer climate and turbulent exchange in the ablation zone of the west Greenland ice sheet, Int. J. Climatol., 29, 2309–2323, doi:10.1002/joc.1815, 2009.

Van den Broeke, M. R., Smeets, C. J. P. P., and van de Wal, R. S. W.: The seasonal cycle and interannual variability of surface energy balance and melt in the ablation zone of the west Greenland ice sheet, The Cryosphere, 5, 377–390, doi:10.5194/tc-5-377-2011, 2011.

Vaughan, D. G., Comiso, J. C., Allison, I., Carrasco, J., Kaser, G., Kwok, R., Mote, P., Murray, T., Paul, F., Ren, J., Rignot, E., Solomina, O., Steffen, K., and Zhang, T.: Observations: Cryosphere, in: Climate Change 2013: The Physical Science Basis, Contribution of Working Group I to the Fifth Assessment Report of the Intergovernmental Panel on Climate Change, edited by: Stocker, T. F., Qin, D., Plattner, G.-K., Tignor, M., Allen, S. K., Boschung, J., Nauels, A., Xia, Y., Bex, V., and Midgley, P. M., Cambridge University Press, Cambridge, UK, New York, NY, USA, 317–382, 2013.

TCD
9, 2867–2913, 2015

Wientjes, I. G. M. and Oerlemans, J.: An explanation for the dark region in the western melt zone of the Greenland ice sheet, The Cryosphere, 4, 261–268, doi:10.5194/tc-4-261-2010, 2010.

Yen, Y. C.: Review of thermal properties of snow, ice and sea ice, Technical report, USA Cold Regions Research and Engineering Laboratory, CRREL Report, Hanover, New Hampshire, USA, 81–10, 1981.

TCD
9, 2867–2913, 2015

Table 1. Sensors and their accuracies according to the issued manuals.

parameter	sensor	accuracy
air pressure	Campbell CS100	2 hPa at −40 to 60 °C
aspirated air temperature	Rotronic MP100H aspirated (Pt100)	0.03 °C at 0 °C
relative humidity	Rotronic MP100H aspirated (HygroClip R3)	1.5 % at 23 °C
shortwave radiation (incoming and reflected)	Kipp & Zonen CNR4 (Pyranometer)	10 % for daily totals
longwave radiation (incoming and emitted)	Kipp & Zonen CNR4 (Pyrgeometer)	10 % for daily totals
wind speed and direction	Young 05103-5	0.3 m s^{-1}; 3°
surface height	Campbell SR50A	10^{-2} m or 0.4 %

TCD
9, 2867–2913, 2015

Table 2. Linear regression parameters for hourly values of KAN_U and S10 AWSs: slope (χ), intercept (ψ), correlation coefficients (R) and root-mean-square deviations (RMSD).

S10-KAN_U	χ	ψ	R	RMSD
$E_S^{\downarrow}$ [a]	1.010	–	0.99	37.25 ($W m^{-2}$)
$E_S^{\uparrow}$ [a]	0.987	–	0.99	24.71 ($W m^{-2}$)
$E_L^{\downarrow}$	1.003	−6.06	0.99	8.92 ($W m^{-2}$)
$E_L^{\uparrow}$	0.990	−0.25	1.00	3.62 ($W m^{-2}$)
T_a	0.995	−0.25	1.00	0.50 (°C)
ambient air pressure	0.990	7.77	1.00	0.45 (hPa)
relative humidity	0.899	10.31	0.91	3.78 (%)
wind speed[a]	0.928	–	0.99	0.66 ($m s^{-1}$)
α_{2010} [b]	–	–	0.93	0.032 (–)
α_{2011} [b]	–	–	0.94	0.028 (–)
α_{2012} [b]	–	–	0.91	0.066 (–)

[a] Regression line forced through zero.
[b] 24 h running averages for the months May until September.

TCD
9, 2867–2913, 2015

Table 3. Annual and summer (June–July–August) average meteorological parameters at KAN_U.

KAN_U	2009[a]	2010	2011	2012	2013[b]
annual averages					
T_a (°C)	−15.5	−11.6	−18.0	−14.3	−15.4
ambient air pressure (hPa)	799	804	797	800	799
specific humidity ($g\,kg^{-1}$)	1.5	2.0	1.4	1.9	1.5
wind speed ($m\,s^{-1}$)	7.0	7.0	6.2	6.5	7.0
albedo	0.85	0.82	0.82	0.79	0.80
summer (JJA) averages					
T_a (°C)	−4.3	−1.8	−2.9	−1.8	−4.5
ambient air pressure (hPa)	809	808	811	811	804
specific humidity ($g\,kg^{-1}$)	2.9	3.6	3.3	3.7	2.8
wind speed ($m\,s^{-1}$)	5.3	5.2	5.0	4.6	5.2
albedo	0.78	0.77	0.78	0.71	0.78

[a] Average 2010–2013 January, February and March.
[b] Average 2009–2012 October, November and December.

TCD
9, 2867–2913, 2015

Table 4. Surface mass budgets (measured in winter and calculated in summer) at KAN_U in m w.e., ablation duration and average ablation rates in mm w.e. day^{-1} assuming snow density of 360 kg m^{-3} (the average density of the uppermost 0.9 m measured on 26 April 2013). This assumption was not needed in 2012 and 2013 when actual density measurements were conducted. The uncertainties of the surface height change and snow density are estimated at 0.2 m and 40 kg m^{-3}, respectively.

	winter budget	summer budget	net budget	ablation period	average ablation rate
2008–2009	+0.59[a] ± 0.15	−0.26 ± 0.08	+0.34[a] ± 0.12	1 Jun–19 Aug	3.25
2009–2010	+0.25 ± 0.08	−0.44 ± 0.09	−0.19 ± 0.12	30 Apr–5 Sep	3.41
2010–2011	+0.37 ± 0.08	−0.41 ± 0.09	−0.04 ± 0.12	28 May–13 Aug	5.26
2011–2012[b]	+0.25 ± 0.08	−0.86 ± 0.14	−0.61 ± 0.16	26 May–24 Aug	9.05
2012–2013[c]	+0.45 ± 0.09	−0.27 ± 0.08	+0.18 ± 0.12	29 May–17 Aug	3.33

[a] Value inferred from Van de Wal et al. (2012).
[b] Estimate based on snow-pit densities from May 2012.
[c] Estimate based on snow-pit densities from May 2013.

TCD
9, 2867–2913, 2015

Table 5. Annual and summer (June–July–August) average energy fluxes at KAN_U ($W m^{-2}$).

	2009[a]	2010	2011	2012	2013[b]
annual averages					
$E_S^{\downarrow}$	155	153	150	145	151
$E_S^{\uparrow}$	−125	−121	−121	−110	−119
E_S^{Net}	30	32	29	35	32
$E_L^{\downarrow}$	207	224	205	223	212
$E_L^{\uparrow}$	−246	−262	−239	−254	−248
E_L^{Net}	−39	−38	−34	−31	−36
E_R	−9	−6	−5	4	−4
E_H	17	18	12	12	14
E_E	−2	−1	−2	−1	−3
E_G	−2	−3	1	−2	−2
E_P	0.004	0.006	0.009	0.012	0.005
E_M	4	8	6	13	5
summer (JJA) averages					
$E_S^{\downarrow}$	322	305	302	296	313
$E_S^{\uparrow}$	−252	−234	−236	−208	−242
E_S^{Net}	70	71	66	88	71
$E_L^{\downarrow}$	237	259	252	260	245
$E_L^{\uparrow}$	−291	−303	−299	−303	−292
E_L^{Net}	−54	−44	−47	−43	−47
E_R	16	27	19	45	24
E_H	6	6	8	7	5
E_E	−9	−9	−7	−5	−13
E_G	2	4	4	2	1
E_P	0.014	0.025	0.035	0.049	0.021
E_M	15	28	24	49	17

[a] Used average 2010–2013 values for January, February and March. [b] Used average 2009–2012 values for October, November and December.

TCD
9, 2867–2913, 2015

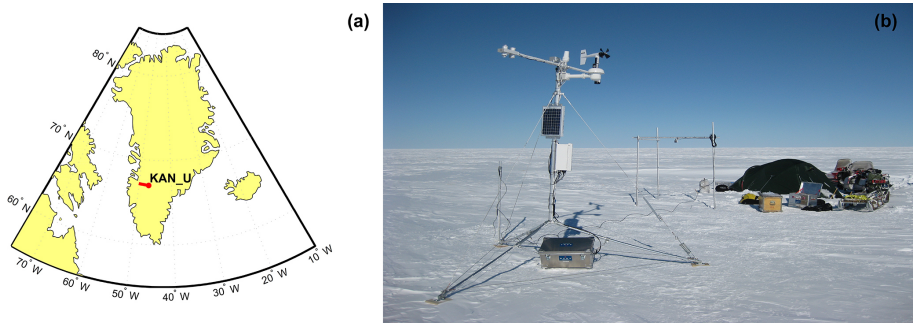

Figure 1. (a) Map of Greenland and the location of KAN_U. **(b)** Picture taken after the installation of KAN_U (April 2009).

TCD
9, 2867–2913, 2015

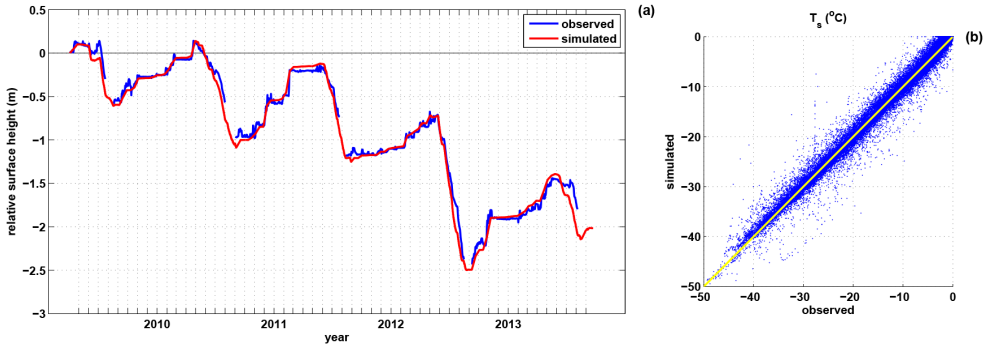

Figure 2. SEB model validation: **(a)** observed and simulated relative surface height for the period of observations. **(b)** Observed against simulated T_s ($R^2 = 0.98$; $(\Delta T_s)_{avg} = 0.11\,^{\circ}C$; RMSE = 1.43 °C).

TCD
9, 2867–2913, 2015

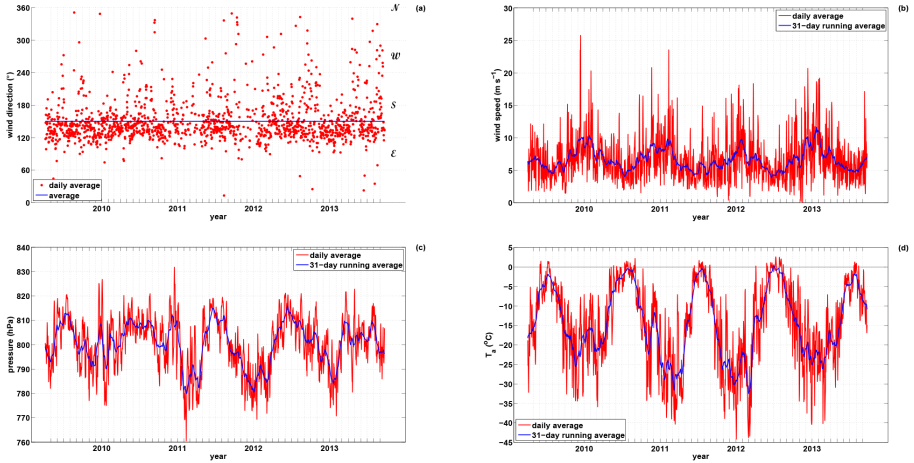

Figure 3. Average values of: **(a)** wind direction, **(b)** wind speed, **(c)** air pressure and **(d)** air temperature at KAN_U.

TCD
9, 2867–2913, 2015

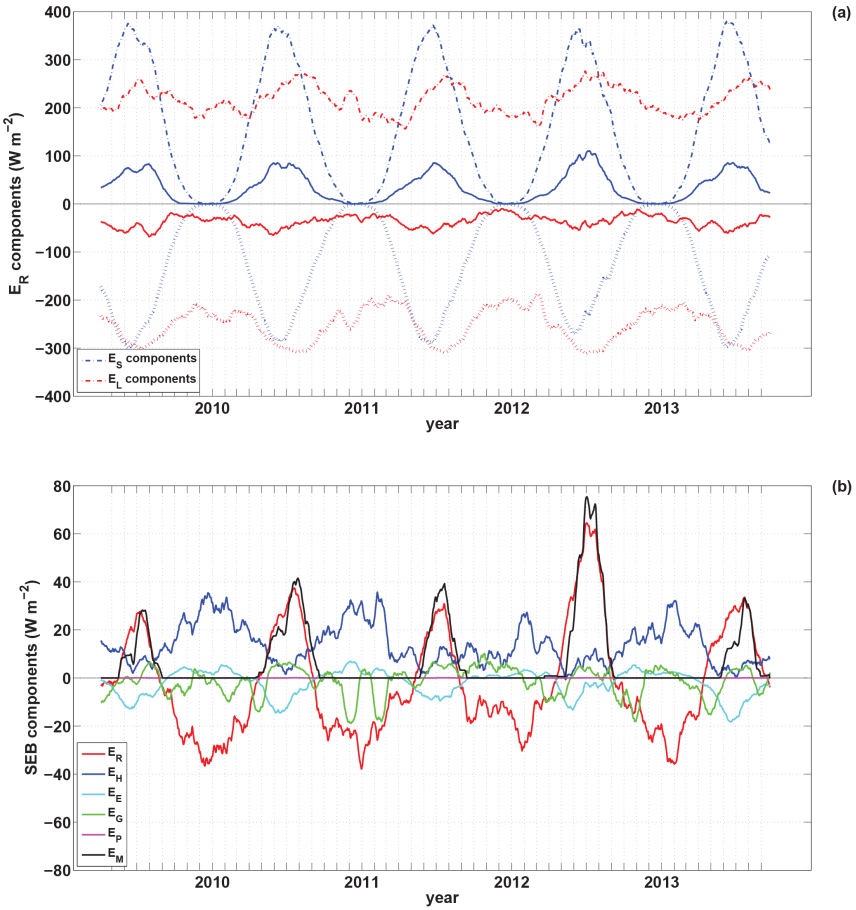

Figure 4. (a) 31 day running average values of all radiation budget components at KAN_U. Solid lines indicate the net solar and terrestrial radiation components. **(b)** Same, as **(a)**, but for all surface energy balance components.

TCD
9, 2867–2913, 2015

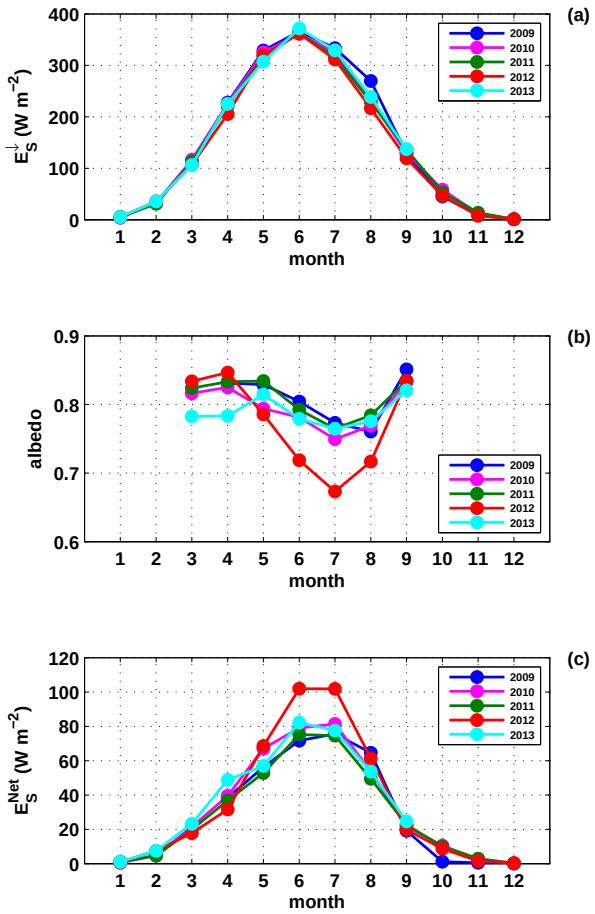

Figure 5. Seasonal cycles for the years 2009–2013 based on monthly averages of: **(a)** incoming shortwave energy flux, **(b)** surface albedo and **(c)** net shortwave energy flux.

TCD
9, 2867–2913, 2015

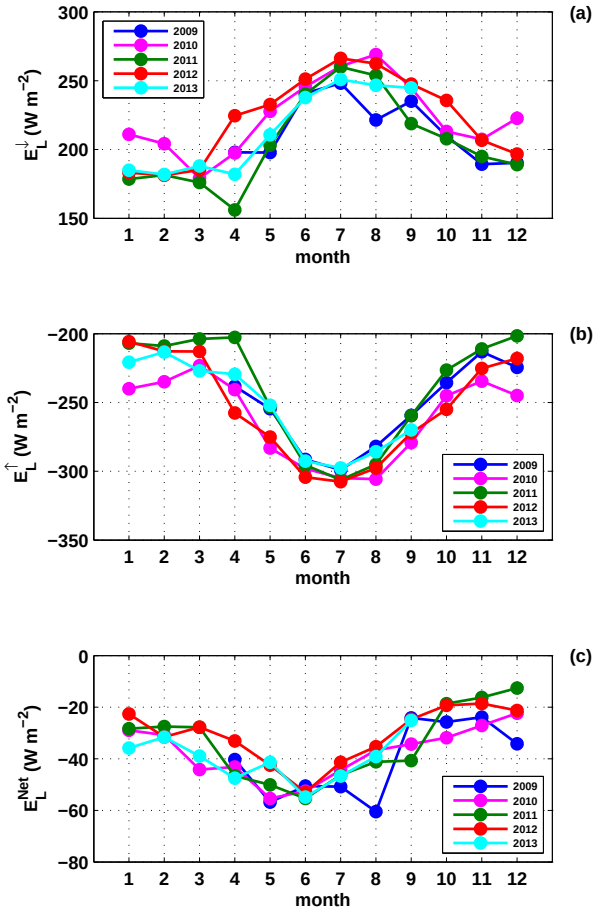

Figure 6. Seasonal cycles for the years 2009–2013 based on monthly averages of: **(a)** incoming, **(b)** emitted and **(c)** net longwave energy flux.

TCD
9, 2867–2913, 2015

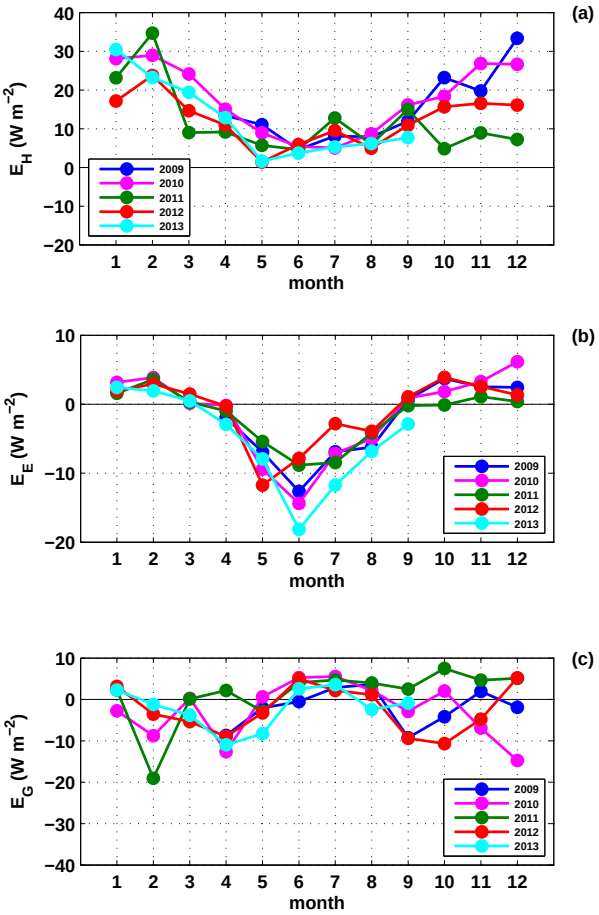

Figure 7. Seasonal cycles for the years 2009–2013 based on monthly averages of: **(a)** sensible heat flux, **(b)** latent heat flux and **(c)** subsurface heat flux.

TCD
9, 2867–2913, 2015

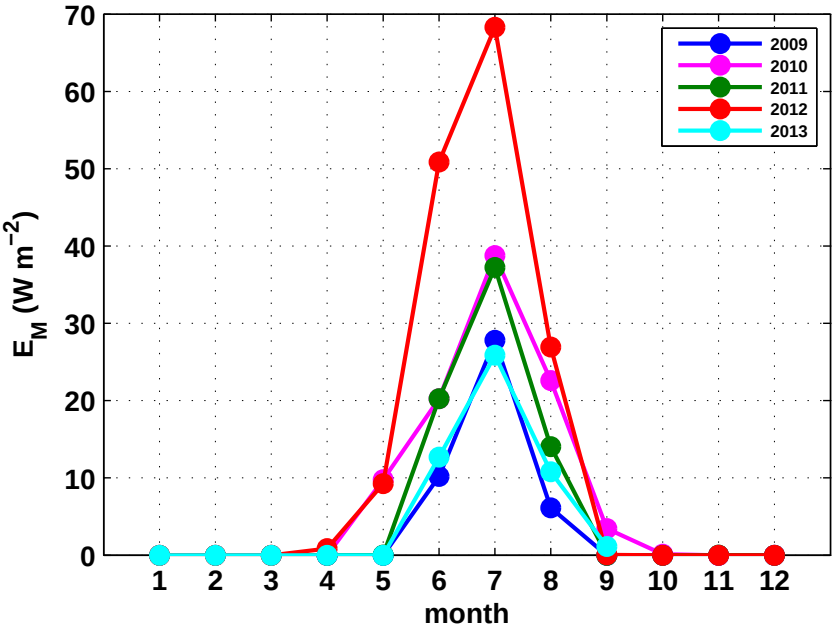

Figure 8. Seasonal cycle for the years 2009–2013 based on monthly averages of energy consumed by melt.

TCD
9, 2867–2913, 2015

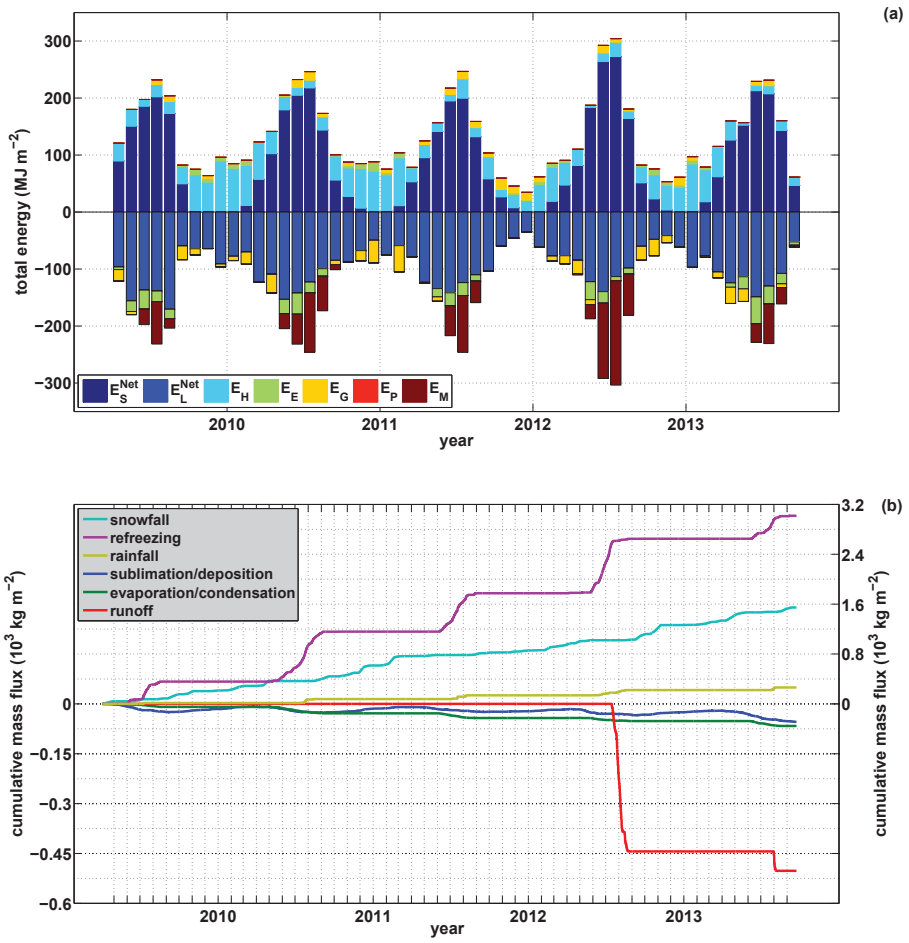

Figure 9. (a) Total energy per unit surface. **(b)** Cumulative fluxes of all mass components. Note the different *y* scales in **(b)**.

TCD
9, 2867–2913, 2015

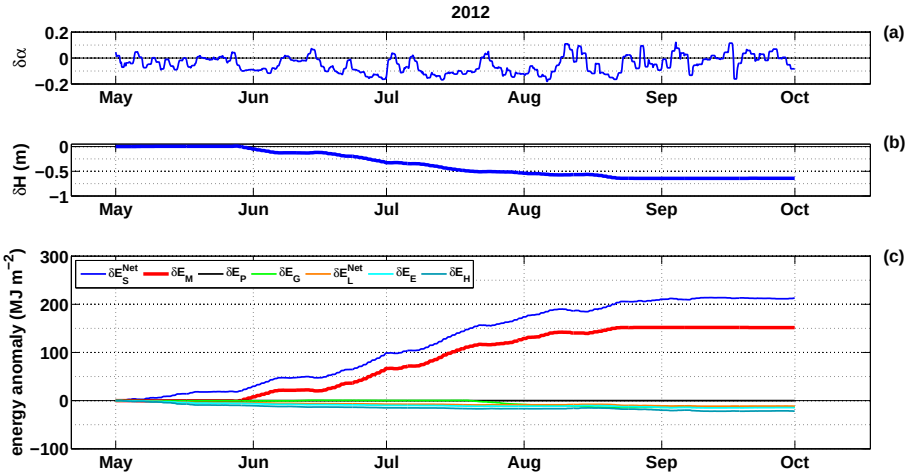

Figure 10. (a) 2012 albedo anomaly measured by KAN_U for the months May–September, **(b)** simulated relative surface height anomaly and **(c)** simulated cumulative energy anomalies for all contributing fluxes.

TCD
9, 2867–2913, 2015

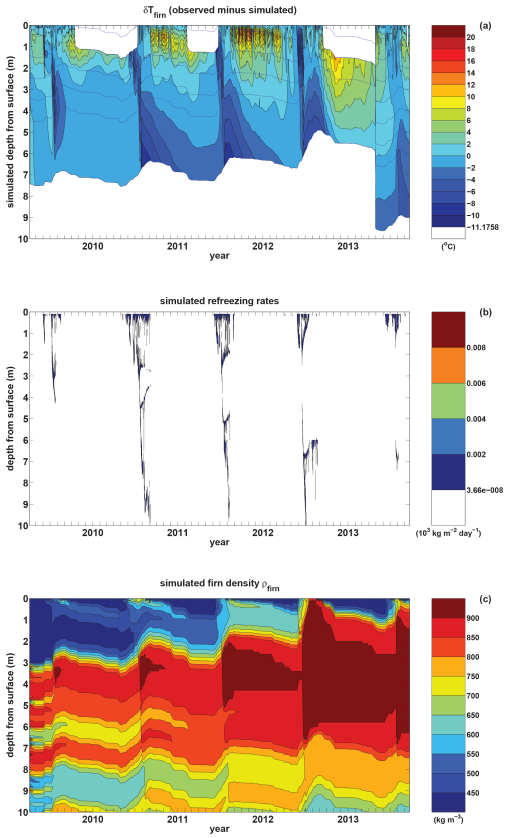

Figure 11. (a) Difference between firn temperature measured by the KAN_U thermistor string and simulated firn temperature. The blue lines indicate the position of the thermistors below the surface. The white areas near the surface are due to surfacing thermistors. Note that the thermistor string was replaced by a new one drilled on 28 April 2013. **(b)** Simulated refreezing rates. **(c)** Simulated firn density.

TCD
9, 2867–2913, 2015

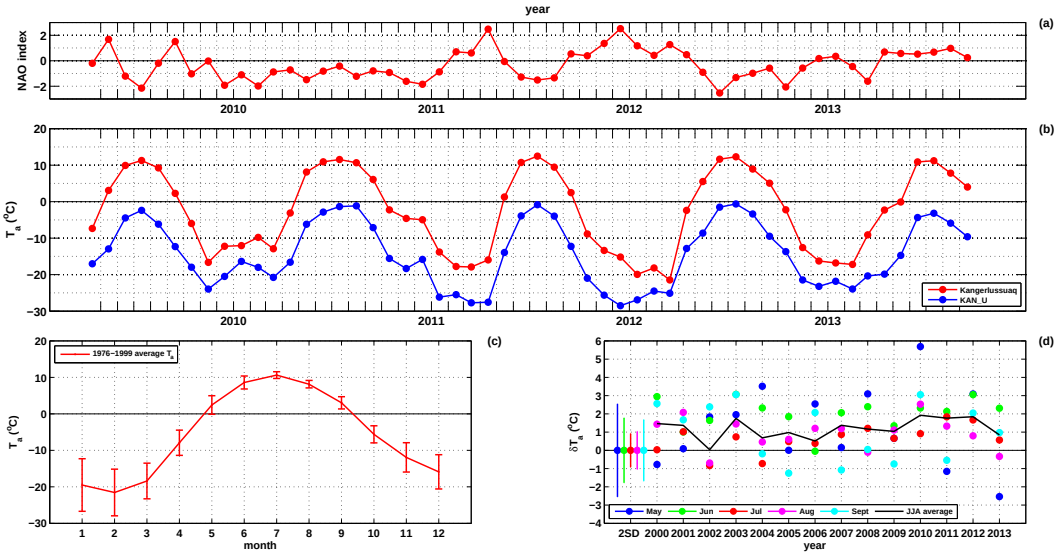

Figure 12. (a) Monthly average NAO index. **(b)** Monthly air temperature from Kangerlussuaq and at KAN U. Correlation coeffcients: 0.97 for the extent of the KAN_U data, 0.66–0.99 for the months individually, minimum being January. **(c)** Monthly reference period (1976–1999) air temperature at Kangerlussuaq. **(d)** Monthly (May to September) and summer (June-July-August average) air temperature anomalies at Kangerlussuaq for the years 2000–2013. Error bars indicate two SDs.

TCD
9, 2867–2913, 2015

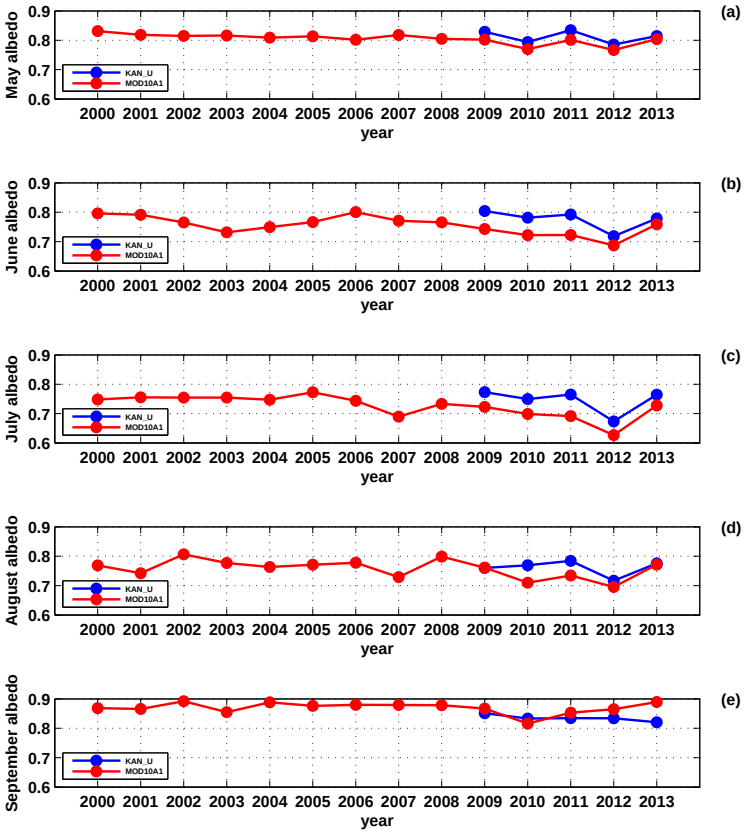

Figure 13. 11 day Gaussian filtered nearest neighbor 5 km × 5 km MOD10A1 albedo (2000–2013) and KAN_U (2009–2013) albedo for the months: **(a)** May (R = 0.91, $(\Delta\alpha)_{avg}$ = −0.02 m, RMSD = 0.02 m), **(b)** June (R = 0.77, $(\Delta\alpha)_{avg}$ = −0.05 m, RMSD = 0.05 m), **(c)** July (R = 0.95, $(\Delta\alpha)_{avg}$ = −0.05 m, RMSD = 0.05 m), **(d)** August (R = 0.60, $(\Delta\alpha)_{avg}$ = −0.03 m, RMSD = 0.04 m) and **(e)** September (R = −0.19, $(\Delta\alpha)_{avg}$ = 0.02 m, RMSD = 0.04 m).

TCD
9, 2867–2913, 2015